Linking multiscale deformation to microstructure in cortical bone using in situ loading, digital image correlation and synchrotron x-ray scattering

Anna Gustafsson[a,*], Neashan Mathavan[a,*], Mikael J Turunen[a,b], Jonas Engqvist[c], Hanifeh Khayyeri[a], Stephen A Hall[c], Hanna Isaksson[a]

[a] Department of Biomedical Engineering, Lund University, Box 118, SE-221 00 Lund, Sweden

[b] Department of Applied Physics, University of Eastern Finland, POB 1627, FI-702 11, Kuopio, Finland

[c] Division of Solid Mechanics, Lund University, Box 118, SE-221 00 Lund, Sweden

[*]shared first authorship.

E-mail addresses: anna.gustafsson@bme.lth.se (A. Gustafsson), neashan.mathavan@bme.lth.se (N. Mathavan), mikael.turunen@uef.fi (M.J. Turunen), jonas.engqvist@solid.lth.se (J. Engqvist), hanifeh.khayyeri@bme.lth.se (H. Khayyeri), stephen.hall@solid.lth.se (S.A. Hall), hanna.isaksson@bme.lth.se (H. Isaksson).

Corresponding author: Hanna Isaksson

Hanna Isaksson, PhD
Department of Biomedical Engineering, Lund University
Box 118, SE-221 00 Lund, Sweden
Tel: +46 (0) 46 222 1749
E-mail: hanna.isaksson@bme.lth.se

ABSTRACT

The incidence of fragility fractures is expected to increase in the near future due to an aging population. Therefore, improved tools for fracture prediction are required to treat and prevent these injuries efficiently. For such tools to succeed, a better understanding of the deformation mechanisms in bone over different length scales is needed. In this study, an experimental setup including mechanical tensile testing in combination with digital image correlation (DIC) and small/wide angle x-ray scattering (SAXS/WAXS) was used to study deformation at multiple length scales in bovine cortical bone. Furthermore, micro-CT imaging provided detailed information about tissue microstructure. The combination of these techniques enabled measurements of local deformations at the tissue- and nanoscales. The orientation of the microstructure relative to the tensile loading was found to influence the strain magnitude on all length scales. Strains in the collagen fibers were 2-3 times as high as the strains found in the mineral crystals for samples with microstructure oriented parallel to the loading. The local tissue strain at fracture was found to be around 0.5%, independent of tissue orientation. However, the maximum force and the irregularity of the crack path were higher when the load was applied parallel to the tissue orientation. This study clearly shows the potential of combining these different experimental techniques concurrently with mechanical testing to gain a better understanding of bone damage and fracture over multiple length scales in cortical bone.

KEYWORDS

mechanical testing, tension, small angle x-ray scattering, wide angle x-ray scattering, digital image correlation, micro-CT

1. INTRODUCTION

The rapidly aging global population is expected to lead to an increased number of fragility fractures due to age-related decline in bone quality and diseases such as osteoporosis [1]. Understanding the pathophysiology of bone is key for estimating the risk of fractures and developing novel treatments. Fracture risk is related to bone tissue characteristics, such as porosity, bone mineral density, composition, and structural integrity across different length scales [2-4]. However, there is little insight into the deformation mechanisms of bone acting at different length scales. Bone as a material is a hierarchical composite made up of a soft organic collagen phase and a stiff inorganic mineral phase [5-7]. It is this structural hierarchy which produces the exceptional strength and toughness properties of bone that outperform the characteristics of its individual constituents [3]. The mineralized collagen fibril is the basic building block of bone tissue and is made up from collagen molecules packed in a staggered configuration (with ~67 nm gap between the molecules) and reinforced with mineral crystals oriented along the fibrils [8]. The fibrils are packed into lamellae that form different tissue types (e.g. trabecular bone or cortical bone with lamellar or Haversian tissue structure) depending on their arrangement at the microscale. For a more detailed description of the hierarchical structure of bone, see for example [5-7]. Additionally, bone is highly anisotropic with spatially varying material parameters due to, e.g., porosity and differences in bone mineral density. Altogether, this makes deformation mechanisms and damage propagation between length scales extremely complex and each length scale requires appropriate analysis methods

The development of new material characterization methods, including access to synchrotron x-ray facilities in recent decades, has opened up new possibilities to study material structures over a range of length scales. With small and wide angle x-ray scattering (SAXS and WAXS), it is possible to study nanoscale features using the characteristic peaks in the scattering profile caused by periodic arrangement of structures such as collagen molecules and the crystal-lattice spacing in the mineral phase. Key information that can be extracted from SAXS and WAXS data include the orientation and spacing of both the collagen fibrils and the mineral crystals [9]. Furthermore, mechanical testing *in-situ* (i.e., concurrently) with SAXS and WAXS can be used to measure deformation on the nanoscale, by analyzing the changes in position of the scattering peaks, simultaneously with measurement of deformation at the tissuescale. Such experiments to study

bone biomechanics at the nanoscale have been presented in a limited number of studies in tension [10-13], compression [14] and bending [15].

In previous studies on bone mechanics using x-ray scattering, deformation at the nanoscale was compared to force-displacement data from mechanical testing at the macroscale. This approach tends to oversimplify the deformation of the bone tissue by assuming a uniform microstructure with homogeneous deformation under loading. To overcome this, the deformation can be monitored locally, e.g., using Digital Image Correlation (DIC), to resolve the spatial strain distribution at the tissue level. DIC has previously been used to determine inhomogeneous deformations of cortical bone under loading at the organ- [16] and microscale [17-19]. Heterogeneity and variation of the microstructural orientation inside the specimen can be reduced by cutting cortical bone test specimens in well-defined orientations relative to the bone anatomy, given that the predominant microstructural orientation is aligned to the long axis of the bone shaft. However, aligning specimens to the anatomical directions on the organ scale is a rather coarse method in defining the tissue microstructure and a high-resolution imaging technique (e.g. micro-CT or stereomicroscopy) is needed to verify, for example, the porosity and the predominant orientation of the microarchitecture [9].

The aim of this study was to investigate if strains at the tissue- and nanoscales in cortical bone are dependent on bone microarchitecture. If this hold true, then the results can serve as the foundation for the development of computational multiscale models to study deformation mechanisms in cortical bone and to improve the fracture risk assessment. Furthermore, we investigated the influence of tissue type (lamellar or Haversian bone) on the deformation at the different length scales. In this study, the combination of mechanical loading *in-situ* with small and wide angle x-ray scattering and DIC was used to capture the deformation in bone specimens across several length scales simultaneously, following an experimental approach developed previously for polymers [20].

2. METHODS

2.1 Sample preparation

Samples were obtained from the diaphysis of bovine femora in orientations parallel and perpendicular to the long axis of the bone and are referred to as longitudinal or transversal

samples respectively (Figure 1A). Sample dimensions of 40 x 20 mm^2 with a thickness of 1 mm were sectioned using a high-precision diamond band saw at low speed and under constant water irrigation (EXAKT 300 CP Diamond Band Saw, Norderstedt, Germany). Symmetric notches of 5 mm radii were machined on both sides of the sample (Figure 1B). Samples were subsequently wrapped in phosphate buffered saline (PBS) soaked gauze and stored at -20°C. Sample surfaces were spray painted with a random speckle pattern with water-based paint for the purposes of DIC with the exception of a 1 mm wide strip of unpainted bone preserved down the center of the sample for SAXS / WAXS measurements to avoid scattering from the paint (Figure 1B).

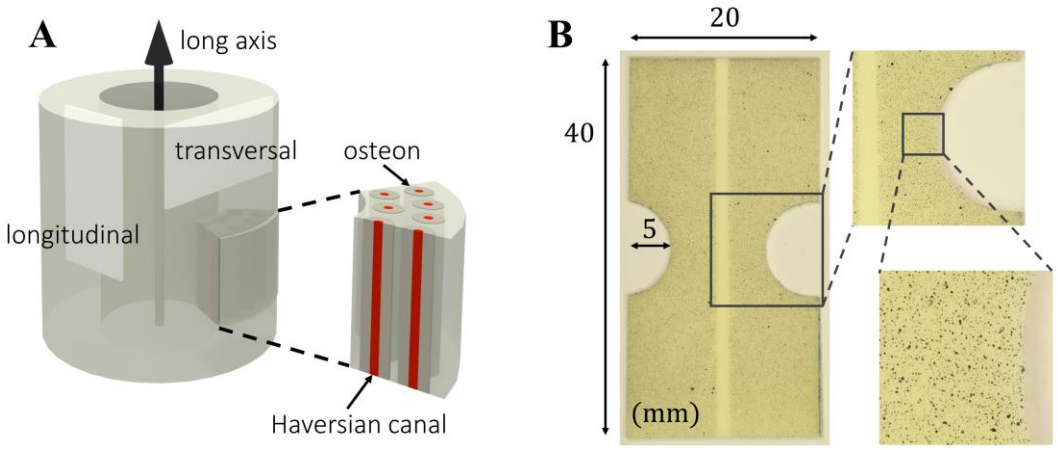

Figure 1: Sample preparation. (A) Samples were taken from the femoral shaft of bovine bone in two different directions to study the effect of the microstructural orientation (i.e., the orientation of the osteons and Haversian canals). The samples are referred to as longitudinal and transversal samples. The sample thickness was 1 mm. (B) Symmetric notches were machined on both sides of the sample and the surface was spray painted with a speckle pattern for DIC. The middle strip was left unpainted for SAXS/WAXS measurements.

2.2 Experimental setup and testing

In-situ loading was performed using a custom-built uni-axial tensile testing device [20]. Axial force and displacement of the grips were recorded by a force transducer and a linear displacement sensor respectively. The device was mounted on a scanning stage at the I911-4 beamline at the MAX II synchrotron (MAX IV Laboratory, Lund University, Lund, Sweden) that enabled rigid vertical translation of the test rig across the X-ray beam [21]. With this setup, SAXS or WAXS data was collected at 10 equally-spaced spatial locations along a 1 mm wide vertical strip of bone (Figure 2).

The mechanical loading was made by a symmetrical displacement, around the centre point of the sample, of the machine grips at 0.005 mm/min . Under continuous loading, photographs were taken of the sample surface using two Prosilica GT6600 29-Megapixel digital cameras with the cameras calibrated for stereo vision. From these photographs the sample surface shape plus the in- and out-of-plane surface deformation of the samples could be obtained by a 3D-surface DIC. SAXS or WAXS intensity patterns were acquired using a 300 x 300 μm^2 synchrotron x-ray beam (λ = 0.91 Å) and an exposure time of 30 s. All images were acquired using a PILATUS 2M detector [22] with sample-to-detector distances of 1950 mm and 395 mm for the SAXS and WAXS setups, respectively. The setup of the DIC system and the SAXS / WAXS acquisition were synchronized such that an image was captured at every instance the x-ray detector acquired data.

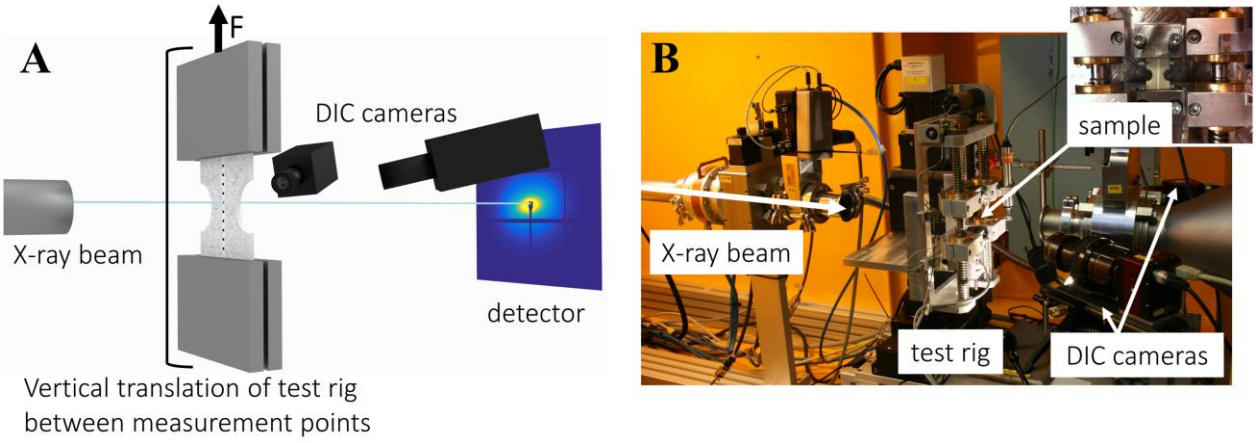

Figure 2: Experimental setup. (A) Schematic illustration of a sample tested in tension and simultaneously monitored with DIC and SAXS or WAXS at 10 discrete vertical positions in the horizontal-centre of the sample. The sample is subjected to continuous tensile loading in the test rig and the whole rig is translated vertically to move the sample between the measurement points inside the beam. (B) Photograph of the experimental setup at the I911-4 beamline (MAX IV Laboratory, Lund University, Lund, Sweden).

2.3 Micro-CT Imaging

After the tensile tests, all samples were imaged using x-ray transmission tomography with the Zeiss Xradia XRM520 tomograph at the 4D Imaging Lab, Lund University. The samples were wrapped in saline soaked gauze during the scans. For all scans, a tube voltage of 80 kV and power of 7 W were used with an exposure time of 5 s per projection for 1601 projections over

360°. The voxel size in the reconstructed images was 9.25 x 9.25 x 9.25 μm^3. The images were centered at the notches of the samples with a field of view of approximately 18x18 mm^2.

Table 1: Overview of tested samples. The sample orientation describes how the samples were cut from the bone shaft (Figure 1A) while the microstructure orientation refers to the actual directions determined from micro-CT images (see Figure 4). The tissue type is based on visual inspection of the micro-CT images and the scattering method describes if the sample was analyzed with SAXS or WAXS. Finally, the abbreviations are used to describe what group each sample belongs to when presenting the assembled data, where T and L denote transversal or longitudinal microstructure and S or W indicate if SAXS or WAXS was used.

Sample	Sample orientation	Microstructure orientation	Tissue type	Scattering method	Abbreviations
1	Transversal	Transversal	Haversian	SAXS	TS
2	Transversal	Transversal	Lamellar	SAXS	TS
3	Transversal	Transversal	Haversian	WAXS	TW
4	Longitudinal	Longitudinal	Haversian	SAXS	LS
5	Longitudinal	Longitudinal	Lamellar	SAXS	LS
6	Longitudinal	Longitudinal	Haversian	SAXS	LS
7	Longitudinal	Longitudinal	Lamellar	SAXS	LS
8	Longitudinal	Radial (out of plane)	Lamellar	WAXS	LW
9	Longitudinal	Radial (out of plane)	Lamellar	WAXS	LW
10	Longitudinal	Heterogeneous	Both	WAXS	TW

The micro-CT images were analyzed using ImageJ v1.50i [23], where the images were realigned using the *interactive stack rotation tool* before they were resliced in the coronal plane. The *minimum intensity projection* was used to visualize the micro-porosity caused by vascular canals

in the tissue and the microstructural orientations were analyzed with the plugin *OrientationJ* [24]. The tissue type was determined by visual inspection and Haversian tissue was found in four out of ten samples with the remaining six samples containing lamellar tissue. The characteristics of all samples are presented in Table 1.

The fractured samples were segmented using SEG3D (version 2.4, CIBC, University of Utah) by applying a manually chosen threshold value. The same threshold value was used for all samples. The crack path was analyzed using a custom-written script implemented in MATLAB® (MATLAB version 2015b, The MathWorks, Inc., Natick, Massachusetts), where the crack length was calculated as the Euclidean distance between all boundary pixels (defined by the built-in function *bwboundaries*) along the crack surfaces. Two measures of crack length were used to quantify the irregularities of the crack paths: (1) the crack length normalized with the notch width and (2) the crack length normalized with the shortest distance between the start and the end point of the crack. For all samples, 54 micro-CT images (corresponding to 0.5 mm thickness) were included where the full crack width was visible. Both crack surfaces (above and below the crack) were analyzed.

2.4 Digital image correlation analysis

The stereovision and stereo-correlation analysis of the sample surface shape plus the in- and out-of-plane surface deformation of the samples, respectively, was performed using the commercial software Vic-3D 7 (Correlated solutions, Columbia, SC, USA). A reference grid was used to calibrate the stereo system, with a resulting calibration error of 0.087 pixels. The calibration error is calculated as the average error in pixels between the actual position of a grid point and the theoretical position according to the calibration model [25]. In the WAXS setup, the lighting unfortunately caused excessive reflections in the images from one of the cameras, which made the correlation impossible and therefore 2D-DIC had to be performed instead using the images from the one remaining camera (Vic-2D 6, Correlated solutions, Columbia, SC, USA). In all analyses, 3D and 2D, a subset size of 125 pixels and a step size of 7 pixels were used in combination with a low pass filter. A Green-Lagrangian spatial decay filter with a radius of 5 pixels was used for strain calculations. The projection error, which is a measure of the correlation accuracy [25], was less than 0.09 pixels for all cases, typically around 0.06 pixels for the 3D-DIC and lower than 0.01 pixels for the 2D-DIC.

To enable comparison with studies where video extensometry have been used to measure strain [11, 12], a virtual extensometer was defined according to Figure 3. The extensometer strain ε_{AB} was calculated as the difference in axial displacement, U, between the regions A and B and divided by the initial length L_0. Additionally, the average surface strains ε_{yy} were calculated inside the notch and referred to as ε_{ROI}.

2.5 SAXS and WAXS analysis

Before any analyses of the SAXS/WAXS data, the beamstop and gaps between detector sectors were masked from the SAXS and WAXS scattering images. All pre-processing and analyses of the SAXS and WAXS data were performed using custom-written scripts in MATLAB® (MATLAB version 2014a, The MathWorks, Inc., Natick, Massachusetts) [26, 27].

From the 2D SAXS detector images, the orientation of the collagen fibers was determined by integrating the scattering pattern azimuthally to obtain the I(θ) curve, i.e. the scattering intensity as a function of the azimuth angle, θ. The intensity peaks from mineral scattering in the I(θ) curve are perpendicular to the predominant orientation of mineral plates and collagen fibers. Subsequently, radial integration using a 15° sector to the direction of the predominant orientation on both sides of the center of the beam was used to obtain the I(q) scattering curves, i.e., scattering intensity as a function of the scattering vector, q. A Gaussian curve was fit to the I(q) data around the 3rd order collagen peak (at ~0.281 nm^{-1}) arising from the ~67 nm periodic structure of collagen. The periodicity of the collagen fibers, i.e. d-spacing, was estimated from the location of the Gaussian peak maximum. The relative change in the periodicity during loading was considered as collagen strain [9, 11]. Furthermore, the predominant orientation of the collagen was determined from the SAXS data following the procedure outlined in [28, 29], where the degree of orientation was described by a value between 0 and 1. Here, 0 indicates no predominant orientation and 1 represents perfectly aligned crystals. The relative change in degree of orientation during loading compared to the unloaded state was calculated and compared to the tissue strain.

The I(q) curves from the WAXS scattering images were obtained by radial integration using the total 360° range about the beam-center in the 2D images. A Gaussian curve was fitted to the (002)-reflection peak of the mineral phase, which is aligned with the c-axis of the mineral crystals and with the orientation of the collagen fibers. The crystallographic lattice spacing of the

mineral phase was determined from the Gaussian peak maximum using Bragg's law. The relative change in lattice spacing during loading compared to the unstressed state was considered as mineral strain [11].

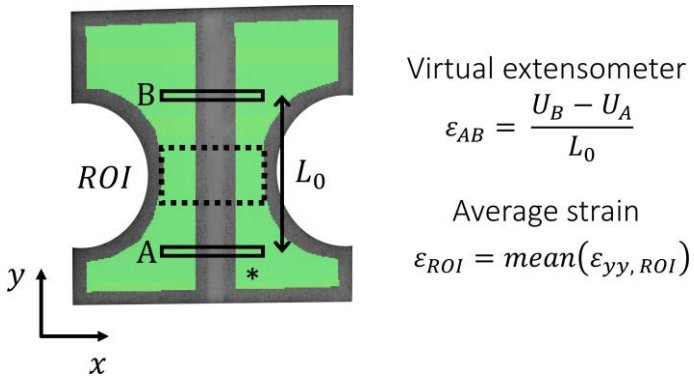

Figure 3: Tissue strain analysis. The green areas mark regions with strain data from the DIC analysis. Note that no DIC analysis could be done in the middle strip that was left unpainted for SAXS and WAXS measurements, and that the width of the empty border surrounding the green areas is determined by the subset size in the DIC analysis. A and B denote two regions representing the start and end points of the virtual extensometer separated by the length L_0 and the dashed rectangle marks the region of interest (ROI) inside the notch where axial strains were averaged. The asterisk sign (*) has been used to indicate what part of the samples was still loaded in tension when partial slip occurred in the grips.

2.6. Data analysis

The samples were divided into four groups depending on microstructural orientation and scattering analysis method (see group abbreviations LS, TS, LW and TW in Table 1). Each time point contained measurements from three length scales: macroscale mechanical test data (tensile force and displacement), tissuescale deformation from DIC (average tissue strain in the notch $\varepsilon_{ROI}*$, see Figure 3) and nanoscale deformation from SAXS or WAXS (strain in collagen or minerals). In each group, the time points were sorted by the tissue strain magnitudes, ranging from 0 up to approximately 0.0025. The time points were divided into bins, defined as 10^{-4} sized intervals of tissue strain, so that the first bin contained all time points with tissue strain values between 0 and 1e-4 etc. All values within each bin were averaged (tensile force, collagen strain and mineral strain) and presented as functions of tissue strain. Data from measurement points 3-8 from the SAXS and WAXS analysis were included, as these were located in the vicinity of the notch, and could therefore be compared to the tissue strain in the notch (Figure 3). Each bin

usually contained about 3-8 time points and bins with only one point were excluded from the analysis to reduce the effect of single points.

3. RESULTS

3.1. Orientations and heterogeneity of the tissue microstructure

The microstructure of the samples was assessed from the micro-CT images, where porosities such as Haversian canals were seen as darker features (Figure 4). In the transversal and longitudinal samples the main fiber orientation was clear, with parallel fibers throughout the samples (Figure 4A-B). For the radial group, the fibers ran in the out-of-plane direction, through the samples' thickness, and were, hence, very short and only seen as dark red spots (Figure 4C). The micro-CT image of the heterogeneous sample displayed two different tissue types with different micro-orientations: Haversian tissue with longitudinal osteons in the lower left part and lamellar tissue with oblique fibers in the right half (Figure 4D).

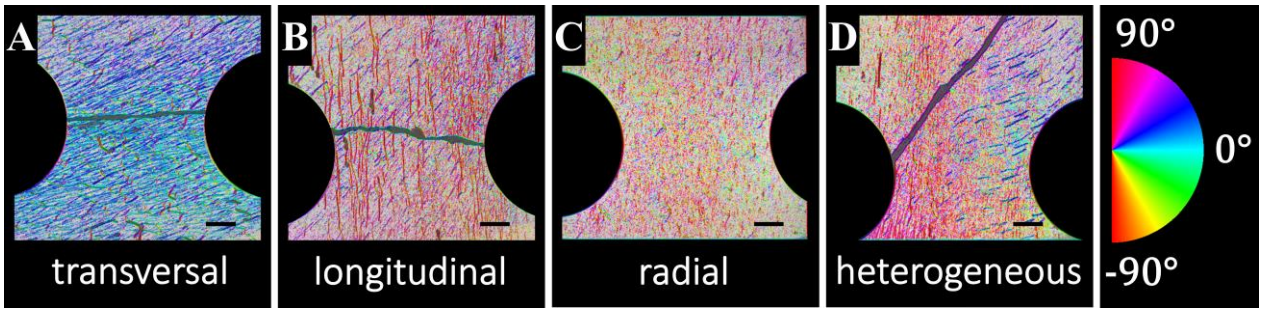

Figure 4: Visualization of the microstructural orientation. The samples were grouped according to the microstructural orientation introduced in Table 1 and samples 1, 6, 8 and 10 are shown as representative samples for each group. The voxel size in the images is 9.25 µm and the scale bars correspond to 2 mm.

The fracture paths followed the fiber orientations in both the transversal and the heterogeneous samples (Figure 4A, D), resulting in smooth and straight crack surfaces (Figure 5A, C). The longitudinal sample had a more irregular crack path (Figure 5) and a higher maximum force compared to the other samples (Table 2).

Table 2: Analysis of fracture paths. Maximum force and crack lengths normalized with respect to the notch width and the shortest distance between the start and end point of the crack for sample 1, 6 and 10.

Microstructural orientation	F_{max} (N)	Crack length normalized with notch width	Crack length normalized with shortest crack distance
Transversal	269	1.095	1.083
Longitudinal	414	1.193	1.166
Heterogeneous	318	1.479	1.111

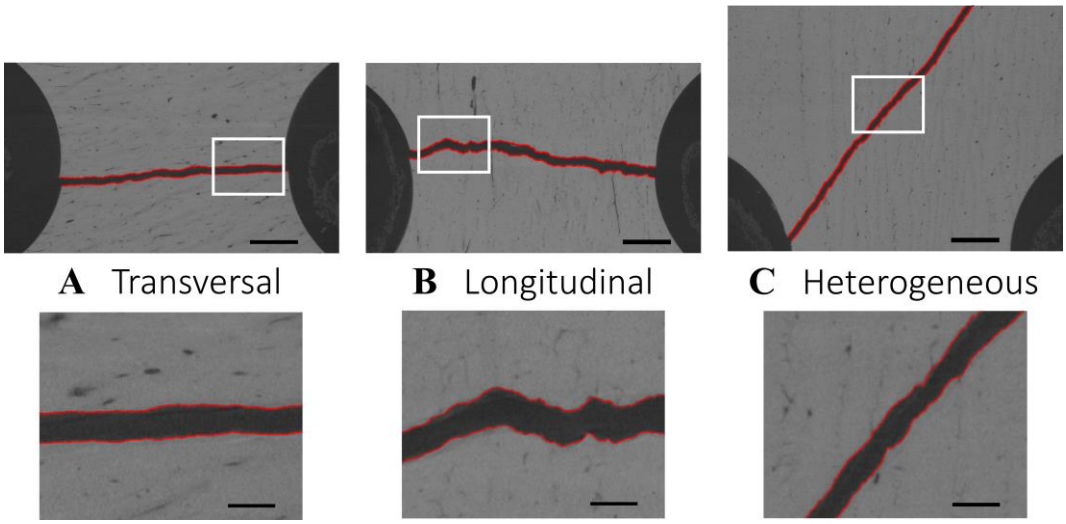

Figure 5: Illustration of fracture paths in three samples with different microstructural orientations (sample number 1, 6 and 10). The white boxes mark the magnified regions and the red lines show the boundary pixels used to calculate the crack length. The sample with longitudinal microstructure had the most irregular crack path. The scale bars in the top row represent 2 mm and the ones in the magnified images in the bottom row represent 500 µm.

3.2. Tissuescale deformation

The DIC analysis of the samples provided information about the local deformation on the sample surfaces. Symmetric strain distributions concentrated around the notches were seen in all except one sample (Figure 6). In all fractured samples, the location of maximum strain in the notch coincided with the crack initiation point (see e.g. Figure 6A). In the heterogeneous sample there was an asymmetric strain distribution concentrated in the lower part of the left notch, which coincided with the region of Haversian bone tissue (Figure 6C). For this sample, the crack

initiated in the region with high strain in the notch and then followed the microstructure, as visualized in Figure 4C. The local tissue strain value at the fracture point was around 0.5% in all samples that were loaded until failure.

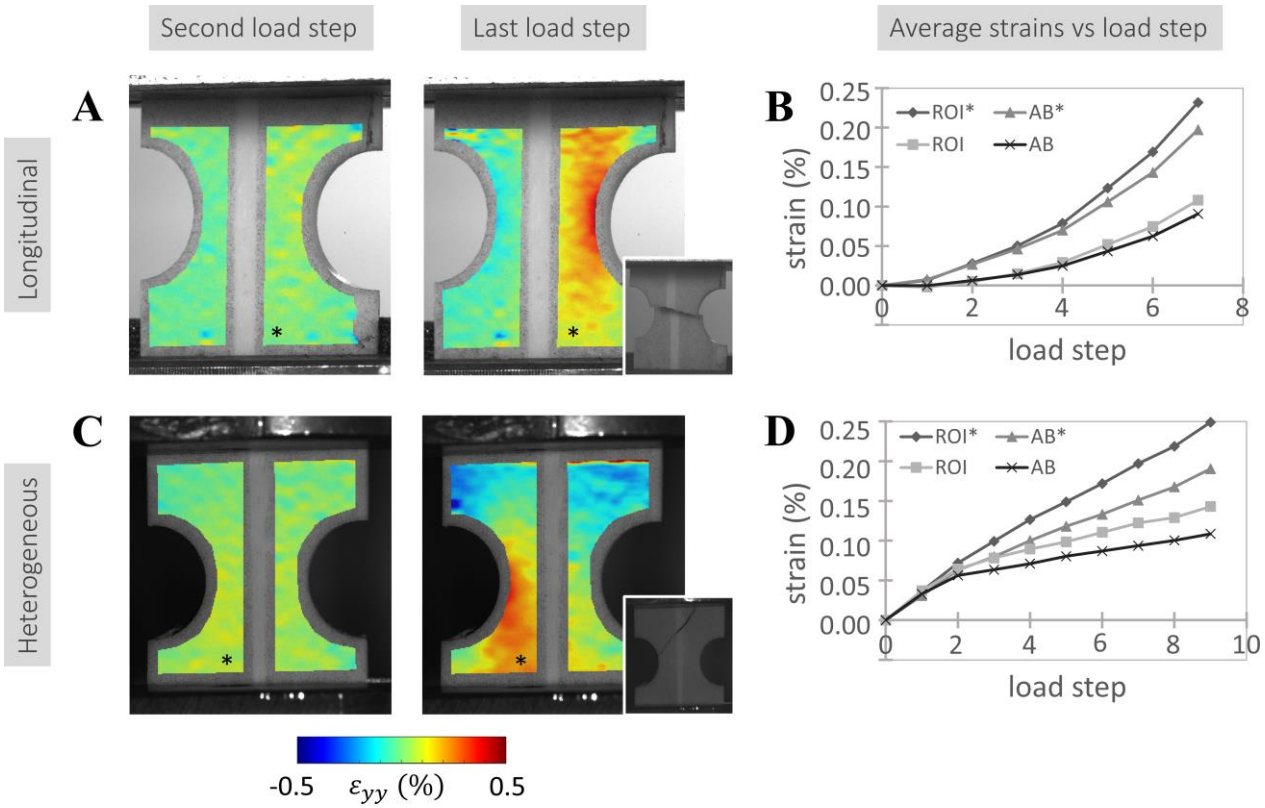

*Figure 6: Surface strains at the tissuescale measured with DIC. The axial surface-strain distributions displayed for a sample with longitudinal microstructure (sample 6) in (A) and a heterogeneous microstructure (sample 10) in (C) from two different time points. Note that the surface strains in (A) was analyzed with 3D-DIC while 2D-DIC was used in (C). The high magnitude strain fields represent the time points just before fracture and photos of the resulting fracture paths are given for comparison. The average strain values, ε_{AB}, calculated with the virtual extensometer and strain values averaged inside the notch region, ε_{ROI}, are shown as a function of the load step for the longitudinal (B) and the heterogeneous (D) sample. *Denotes the side in tension when the samples partly slipped.*

The notch strain ε_{AB}, calculated using the virtual extensometer, exhibited values that were slightly lower than the averaged strains inside the notch ε_{ROI} (Figure 6B, D). A bigger difference was found when comparing the results from the side that was fixed (see * in Figure 6) to values from the full sample width (most clearly seen in the left side of Figure 6A, and also noticeable in the right side of Figure 6C). However, the local DIC analysis showed there was still tension in

half of the sample and therefore ε_{ROI}* will be used as a measure of the tissue strain in section 3.4., when comparing tissue- and nanoscale deformations.

3.3. Deformation on the nanoscale

Deformation in both the collagen and mineral phase were observed with loading, with 2-3 times higher strains in the collagen compared to the mineral (Figure 7).

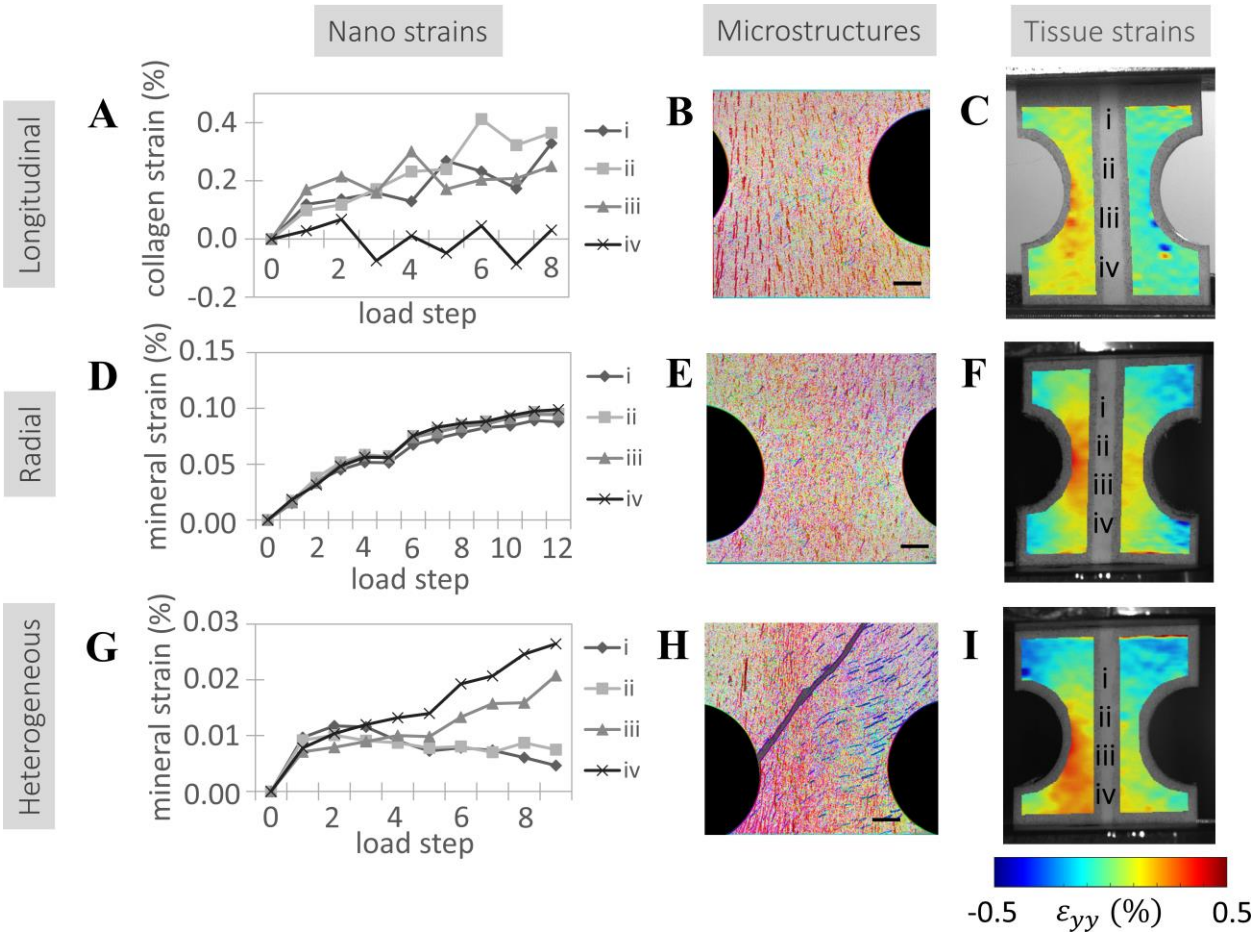

Figure 7: Local deformations at the nano- and tissuescale compared to microstructure. Typical in situ measurements from SAXS and WAXS showing strains in collagen (A) and minerals (D and G) at each load step, to be compared with the microstructural orientations (B, E, H) and the tissuescale surface strains (C, F, I) analyzed with DIC at the last load step before fracture. Collagen and mineral strains in (A, D, G) are given at four points (i-iv) and their approximate locations are marked on the samples in (C, F, I). The nano strain values are calculated as average values between two neighboring measurement points. Scale bars in the micrographs (B, E, H) represent 2 mm.

In general, the microstructure orientation seemed to influence the strain distributions both on tissue- and nanoscale (Figure 7). Consequently, samples with a more homogeneous microstructure showed more homogeneous strain distributions on both tissue- and nanoscales (see Figure 7A where points i-iii showed comparable collagen strains around 0.2%, and Figure 7D, where mineral strains around 0.01% were found in all measurement points). In the samples with a more heterogeneous microstructure, higher mineral strains were found in regions where the microstructure was oriented parallel to the load direction, compared to regions where the microstructure had an oblique orientation (Figure 7G-H). Overall, the mineral strains in the heterogeneous sample were considerably lower than in the homogeneous sample.

Figure 8 shows the data points from all samples organized relative to the grouping in Table 1. A linear force-strain behavior was found in all groups where the transversal WAXS samples had lower stiffness (interpreted from the slopes of the force-strain curves) compared to the other groups and the transversal SAXS samples were less stiff than the longitudinal SAXS samples and equally stiff as the longitudinal WAXS samples.

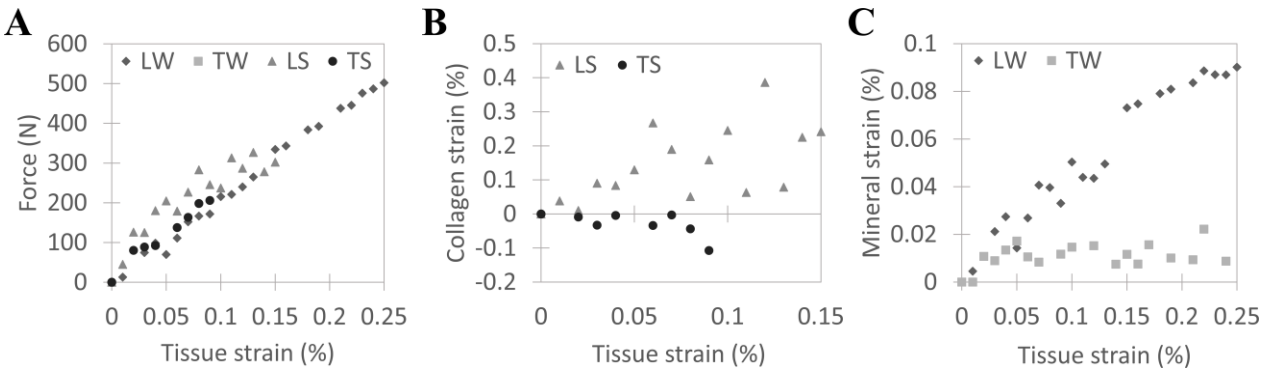

Figure 8: Multiscale mechanical testing. (A) The tensile force from the mechanical testing as a function of tissue strain (ε_{ROI}) in the notch (described in Figure 3), with samples grouped according to tissue orientation and scattering analysis method (SAXS or WAXS, see Table 1). The strains in collagen (B) and minerals (C) as a function of tissue strain (ε_{ROI}*) are shown for all sample groups. Measurement points 3-8 from SAXS and WAXS analysis were included in the analysis.*

The orientation of the microstructure had a large influence on the strains in both collagen fibers and mineral crystals, with higher strains in both cases for samples loaded along the fiber directions (longitudinal). The SAXS data were noisier than the WAXS data, however it was possible to determine that the strains in the transverse collagen fibers stayed close to zero or

became slightly negative when loaded, while the strains in the longitudinal collagen fibers increased and appeared to reach a plateau around 0.2% strain. The WAXS data showed more clearly that the strains increased linearly in the mineral crystals with respect to tissue strain in longitudinal crystals up to a maximum values around 0.1%. In the transverse mineral crystals there was a low initial strain around 0.01%, however the mineral strain did not increase beyond this point when the tissue strain increased.

4. DISCUSSION

Our results show that the orientation of the cortical bone microstructure, relative to the direction of tensile loading, has great impact on the strain magnitudes at both tissue- and nanoscale. On the nanoscale, higher strains were found in both collagen and minerals when they were oriented parallel to the direction of tensile loading, compared to nanostructures oriented perpendicular or oblique to the loading direction. Furthermore, in longitudinal samples, the strain magnitudes in collagen were 2-3 times higher compared to the mineral strains, which is consistent with reported values for tension [11] and compression [14]. However, the deformation mechanisms in collagen and minerals seem to be different. Continuous increase in mineral crystal deformation was observed with increasing tensile load, whereas an initial deformation that seemed to stabilize at higher loads was observed in the collagen fibers. The effect of microstructural orientation was also seen on the global level, where samples oriented parallel to the load showed higher global stiffness compared to transversely oriented samples. Comparable magnitudes of local tissue strains, around 0.5%, were found at the fracture initiation points in the different samples and this was found to be independent of tissue orientation. However, the final crack paths differed depending on tissue microstructure and generally followed the local microstructure orientation.

With the SAXS and WAXS techniques, strains on the nanoscale were calculated along the collagen fibers and the mineral c-axis, regardless of load direction. In the heterogeneous sample (Figure 7G-I), the strain magnitude in the minerals seemed to depend on the angle between the microstructure and the load, so that only the force component parallel to the crystals contributed to the measured deformation. As a consequence, no increase in strain was seen in the transversely oriented minerals where the load was applied perpendicular to the crystals (Figure 8C and also Figure 7G-I, points i and ii). However, there was an initial increase in strain also in the

transversal minerals, which could originate from reorganization in the tissue when the load was first applied. In the case of the transverse collagen fibers (Figure 8B), no or very low negative strains were measured, which could be caused by the collagen fibers bulging when loaded in the transverse direction. To the authors' best knowledge, no previous study looked at the deformation in collagen and minerals in samples loaded in the transverse direction and more studies are needed to clarify the deformation and damage mechanisms in this configuration. Computational multiscale models could potentially be used to clarify for example the relations between micro-orientation and deformation in collagens and minerals, as these effects are difficult to separate experimentally.

Results from DIC analysis displayed inhomogeneous strain patterns on the sample surfaces (Figure 6). The average tissue strain values reported here are in the same order of magnitude as the collagen fiber strains (Figure 8B). Locally, in the notch, higher tissue strains up to 0.5% were found, but as these were located away from the SAXS/WAXS measurement points, averaged tissue strain values were used to compare with nanoscale strains measured in the middle of the samples. In a previous study, tissue strains were reported to be more than twice as high as the collagen strains [11]. There could be several reasons for the difference when comparing to our findings, e.g. sample geometry or test protocol.

The microstructural orientation clearly influenced the crack patterns in the samples (Figure 5), where the longitudinal sample had the most irregular crack. The heterogeneous sample had the longest crack path (Table 2, crack length normalized with notch width), however, the crack surface followed the microstructure, quite smoothly similar to what can be observed in the transversal sample, which did not increase the fracture resistance of the tissue. To quantify the irregularities of the crack paths, the crack lengths were normalized with the shortest crack distance between the start and the end points of the crack. This analysis confirmed that the longitudinal sample had the most irregular crack path, which increased the fracture resistance and resulted in the highest force at fracture. These results are in agreement with previous studies where crack deflections have been pointed out as one of the most powerful toughening mechanism active at the microscale [30, 31].

Two main observations were made when making the distinction between Haversian and lamellar bone tissue. The first and most noticeable difference was that the tissue type seemed to influence

the mineralized fibril orientation (analyzed from SAXS data) when longitudinal samples were loaded. In this case, the change in degree of orientation of the fibrils was around 2% in Haversian tissue while the degree of orientation in lamellar bone tissue seemed to be less affected by loading (Figure 9). No difference between different tissue types was found for transversal samples, where the reorientation was negligible for both groups. No differences that could be linked to tissue type were found in the other parameters from the SAXS or WAXS analyses (Figure 8). This study only contained a few samples of each tissue type and more experiments are needed to verify the results further.

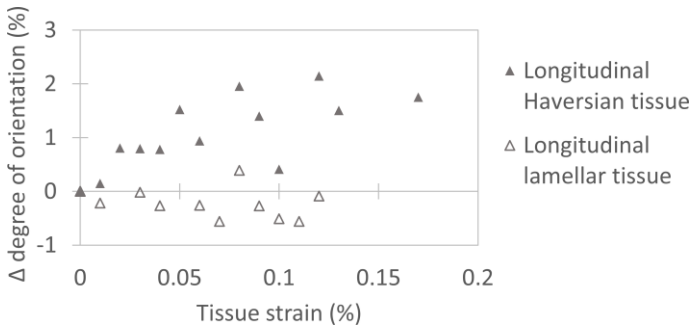

Figure 9: Effects of tissue type. Haversian and lamellar bone seem to react differently to loading in terms of fiber reorientation on the nanoscale. The change in degree of orientation (from SAXS) is shown as a function of tissue strain and reorientation is seen mostly in Haversian longitudinal bone tissue. Four samples from the SAXS analysis, two with lamellar and two with Haversian tissue, were included.

The second main observation, between Haversian and lamellar bone tissue, comes from the DIC-analysis of the heterogeneous sample (Figure 6). A region with high strains was found in the lower part of the notch that visual inspection of the micro-CT images revealed corresponded to Haversian tissue while the rest of the sample contained lamellar tissue. The higher local deformations in the Haversian tissue could be explained by lower stiffness in this tissue type compared to lamellar bone [32].

One key challenge in this study was the sample preparation for the mechanical testing due to the complex and varying structure of cortical bone and because the bovine femur contains both Haversian and lamellar bone. Mayya et al. characterized the anatomic variation of microstructures in bovine femoral cortices and reported that Haversian tissue is found mostly in the posterior parts while the anterior cortex is composed of lamellar tissue [33]. This could explain the different tissue types in the current study (Table 1), which are different from human

femoral cortices that contain primarily Haversian tissue [34]. For this reason, tissue from the posterior region of the bovine femur cortex would have been preferable as it better resembles human cortical bone tissue. However, for proof of concept of the DIC and SAXS/WAXS methodology, bovine tissue was very useful and future work will be to apply the method to human cortical bone tissue.

The micro-CT images highlighted the tissue microstructure and, thus, helped to explain, for example, the unusual crack path in one sample that turned out to be highly heterogeneous. These data also helped to explain the lower global stiffness found in the longitudinal samples where the microstructure was oriented in the out-of-plane direction (WL samples that were characterized as radial). These observations exemplify the difficulty in preparing samples based on anatomical directions and that actual micro-orientation is a better feature for dividing samples into different groups than only cutting direction.

Samples partly slipping in the grips during the loading, and therefore not breaking, was an issue in a number of tests. Unfortunately, this was the case for both samples with radial microstructure and as a consequence no fracture path can be displayed for the radial sample in figure 5. The slipping can have several origins, but the two most likely in this study are subtle variation in sample thickness and surface dehydration during the time inside the SAXS or WAXS hutch. However, both mechanical testing and SAXS/WAXS showed that the samples were still under loading also after the partial slip, which was confirmed from the DIC analysis. Unfortunately, DIC images from one camera had to be excluded for the WAXS samples, which points to the importance of good illumination of the sample when performing DIC; this includes sufficient lighting and avoidance of excessive reflections from the sample surface, both of which will diminish the possibility for correlation of the images. However, only small differences were found when comparing 2D- and 3D-DIC on the SAXS samples, providing confidence that the tissue strain measurements on the WAXS samples with 2D-DIC are reliable.

Due to the experimental setup at the I911-4 beamline (MAX IV), it was not possible to do SAXS and WAXS simultaneously on the same sample. This is a limitation of our study, but this is already possible at other synchrotron beamlines. The results also show more noise in the SAXS data compared to the WAXS data that could be attributed to a weaker signal in the SAXS

measurements or to the fact that the SAXS and WAXS measurements were made during separate experiments.

In summary, an experimental method combining *in-situ* SAXS/WAXS with DIC and mechanical testing was adopted to study deformations over several length scales simultaneously and compare these to the microstructural orientation visualized with high resolution micro-CT. The results indicate that strains on both tissue- and nanoscale depend on the microstructure and illustrate its loadbearing function in cortical bone. Perhaps most importantly, this study demonstrates the potential of an experimental setup where different measurement techniques are combined to enable mapping of local deformations at several hierarchical levels to improve our understanding of multiscale deformation in cortical bone.

Acknowledgements

This work was supported by the Swedish Foundation for Strategic Research [IB2013-0021] and Academy of Finland [project 286091]. The authors would like to acknowledge the MAX IV laboratory, Lund, Sweden for providing the beamtime at the I911-4 beamline and the beamline scientists Sebastian Lages and Ana Labrador for assisting with our experiments, as well as the 4D Imaging Lab, Division of Solid Mechanics, Lund University, for the microtomography imaging.

References

[1] A. Oden, E. McCloskey, J. Kanis, N. Harvey, H. Johansson, Burden of high fracture probability worldwide: secular increases 2010–2040, Osteoporosis International 26(9) (2015) 2243-2248.

[2] E. Donnelly, Methods for assessing bone quality: a review, Clinical Orthopaedics and Related Research® 469(8) (2011) 2128-2138.

[3] P. Fratzl, H. Gupta, E. Paschalis, P. Roschger, Structure and mechanical quality of the collagen–mineral nano-composite in bone, Journal of materials chemistry 14(14) (2004) 2115-2123.

[4] C. Hernandez, T. Keaveny, A biomechanical perspective on bone quality, Bone 39(6) (2006) 1173-1181.

[5] J.-Y. Rho, L. Kuhn-Spearing, P. Zioupos, Mechanical properties and the hierarchical structure of bone, Medical engineering & physics 20(2) (1998) 92-102.

[6] S. Weiner, H.D. Wagner, The material bone: structure-mechanical function relations, Annual Review of Materials Science 28(1) (1998) 271-298.

[7] R. Wang, H.S. Gupta, Deformation and fracture mechanisms of bone and nacre, Annual Review of Materials Research 41 (2011) 41-73.
[8] E.A. McNally, H.P. Schwarcz, G.A. Botton, A.L. Arsenault, A model for the ultrastructure of bone based on electron microscopy of ion-milled sections, PLoS One 7(1) (2012) e29258.
[9] A. Karunaratne, N.J. Terrill, H.S. Gupta, Synchrotron X-ray nanomechanical imaging of mineralized fiber composites, Methods Enzymol 532 (2013) 415-473.
[10] E.A. Zimmermann, B. Gludovatz, E. Schaible, B. Busse, R.O. Ritchie, Fracture resistance of human cortical bone across multiple length-scales at physiological strain rates, Biomaterials 35(21) (2014) 5472-5481.
[11] H.S. Gupta, J. Seto, W. Wagermaier, P. Zaslansky, P. Boesecke, P. Fratzl, Cooperative deformation of mineral and collagen in bone at the nanoscale, Proceedings of the National Academy of Sciences 103(47) (2006) 17741-17746.
[12] H.S. Gupta, W. Wagermaier, G.A. Zickler, J. Hartmann, S.S. Funari, P. Roschger, H.D. Wagner, P. Fratzl, Fibrillar level fracture in bone beyond the yield point, International Journal of Fracture 139(3) (2006) 425-436.
[13] A. Karunaratne, C.R. Esapa, J. Hiller, A. Boyde, R. Head, J. Bassett, N.J. Terrill, G.R. Williams, M.A. Brown, P.I. Croucher, Significant deterioration in nanomechanical quality occurs through incomplete extrafibrillar mineralization in rachitic bone: Evidence from in‐situ synchrotron X‐ray scattering and backscattered electron imaging, Journal of Bone and Mineral Research 27(4) (2012) 876-890.
[14] X.N. Dong, J.D. Almer, X. Wang, Post-yield nanomechanics of human cortical bone in compression using synchrotron X-ray scattering techniques, Journal of biomechanics 44(4) (2011) 676-682.
[15] A. Karunaratne, A. Boyde, C. Esapa, J. Hiller, N. Terrill, S. Brown, R. Cox, R. Thakker, H. Gupta, Symmetrically reduced stiffness and increased extensibility in compression and tension at the mineralized fibrillar level in rachitic bone, Bone 52(2) (2013) 689-698.
[16] L. Grassi, S.P. Väänänen, S.A. Yavari, J.S. Jurvelin, H. Weinans, M. Ristinmaa, A.A. Zadpoor, H. Isaksson, Full-field strain measurement during mechanical testing of the human femur at physiologically relevant strain rates, Journal of biomechanical engineering 136(11) (2014) 111010.
[17] T. Tang, V. Ebacher, P. Cripton, P. Guy, H. McKay, R. Wang, Shear deformation and fracture of human cortical bone, Bone 71 (2015) 25-35.
[18] O.L. Katsamenis, H.M. Chong, O.G. Andriotis, P.J. Thurner, Load-bearing in cortical bone microstructure: Selective stiffening and heterogeneous strain distribution at the lamellar level, Journal of the mechanical behavior of biomedical materials 17 (2013) 152-165.

[19] D.P. Nicolella, D.E. Moravits, A.M. Gale, L.F. Bonewald, J. Lankford, Osteocyte lacunae tissue strain in cortical bone, Journal of biomechanics 39(9) (2006) 1735-1743.
[20] J. Engqvist, S. Hall, M. Wallin, M. Ristinmaa, T. Plivelic, Multi-scale measurement of (amorphous) polymer deformation: simultaneous X-ray scattering, digital image correlation and in-situ loading, Experimental Mechanics 54(8) (2014) 1373-1383.
[21] A. Labrador, Y. Cerenius, C. Svensson, K. Theodor, T. Plivelic, The yellow mini-hutch for SAXS experiments at MAX IV Laboratory, Journal of Physics: Conference Series, IOP Publishing, 2013, p. 072019.
[22] B. Henrich, A. Bergamaschi, C. Broennimann, R. Dinapoli, E. Eikenberry, I. Johnson, M. Kobas, P. Kraft, A. Mozzanica, B. Schmitt, PILATUS: A single photon counting pixel detector for X-ray applications, Nuclear Instruments and Methods in Physics Research Section A: Accelerators, Spectrometers, Detectors and Associated Equipment 607(1) (2009) 247-249.
[23] C.A. Schneider, W.S. Rasband, K.W. Eliceiri, NIH Image to ImageJ: 25 years of image analysis, Nature methods 9(7) (2012) 671-675.
[24] Z. Püspöki, M. Storath, D. Sage, M. Unser, Transforms and operators for directional bioimage analysis: a survey, Focus on Bio-Image Informatics, Springer2016, pp. 69-93.
[25] CorrelatedSolutions, Vic-3D 2010 Reference Manual. <http://www.correlatedsolutions.com/installs/Vic-3D-2010-manual.pdf>, 2010 (accessed 19/12/2017.).
[26] M.J. Turunen, J.D. Kaspersen, U. Olsson, M. Guizar-Sicairos, M. Bech, F. Schaff, M. Tägil, J.S. Jurvelin, H. Isaksson, Bone mineral crystal size and organization vary across mature rat bone cortex, Journal of structural biology 195(3) (2016) 337-344.
[27] M.J. Turunen, H. Khayyeri, M. Guizar-Sicairos, H. Isaksson, Effects of tissue fixation and dehydration on tendon collagen nanostructure, Journal of Structural Biology (2017).
[28] M.J. Turunen, S. Lages, A. Labrador, U. Olsson, M. Tägil, J.S. Jurvelin, H. Isaksson, Evaluation of composition and mineral structure of callus tissue in rat femoral fracture, Journal of biomedical optics 19(2) (2014) 025003-025003.
[29] P. Fratzl, M. Groschner, G. Vogl, H. Plenk, J. Eschberger, N. Fratzl‐Zelman, K. Koller, K. Klaushofer, Mineral crystals in calcified tissues: a comparative study by SAXS, Journal of Bone and Mineral Research 7(3) (1992) 329-334.
[30] R. Nalla, J. Stölken, J. Kinney, R. Ritchie, Fracture in human cortical bone: local fracture criteria and toughening mechanisms, Journal of biomechanics 38(7) (2005) 1517-1525.

[31] K.J. Koester, J.A. Iii, R. Ritchie, The true toughness of human cortical bone measured with realistically short cracks, Nature materials 7(8) (2008) 672.
[32] S.F. Lipson, J.L. Katz, The relationship between elastic properties and microstructure of bovine cortical bone, Journal of biomechanics 17(4) (1984) 231237-235240.
[33] A. Mayya, A. Banerjee, R. Rajesh, Haversian microstructure in bovine femoral cortices: an adaptation for improved compressive strength, Materials Science and Engineering: C 59 (2016) 454-463.
[34] M.L. Hillier, L.S. Bell, Differentiating human bone from animal bone: a review of histological methods, Journal of forensic sciences 52(2) (2007) 249-263.